Supplementary Material

Real-time probing of chirality during a chemical reaction

Denitsa Baykusheva, Daniel Zindel, Vít Svoboda, Elias Bommeli,
Manuel Ochsner, Andres Tehlar, and Hans Jakob Wörner
ETH Zürich, Laboratory of Physical Chemistry, 8039, Zurich, Switzerland

(Dated: November 2, 2019)

www.pnas.org/cgi/doi/10.1073/pnas.1907189116

CONTENTS

I. DETAILS ON DATA ACQUISITION AND ANALYSIS

A. Experimental setup

The excitation pulses are generated by sum-frequency-mixing of the fundamental (Ti:Sa, 800 nm, 1 kHz, 30 fs) and its second harmonic (400 nm) in a type-I-BBO crystal of 50 μm thickness and subsequently compressed in a chirped-mirror assembly, reaching a pulse duration of $\sim$ 40 fs as estimated via cross-correlation. The 1800 nm pulses are produced by frequency up-conversion of an 800 nm seed in a commercial optical parametric amplifier and are subsequently frequency-doubled in a 250 μm type-I-BBO crystal. The polarization of the two orthogonally polarized pulses is converted to bi-circular using the in-line setup (MAZEL-TOV) described in [1]. The pump beams and the bichromatic probe are focussed into the chamber with the aid of an Al-mirror. The generated HH radiation is dispersed by an XUV grating and detected with the aid of an MCP detector backed up with a phosphor screen.

Typical spectrally-resolved far-field HHG images recorded in (*rac*)-2-iodobutane are shown in Fig. S1. Prior to the arrival of the pump pulse (panel a), the spectrum corresponds to the characteristic harmonic comb composed of pairs of neighbouring harmonics ($3q+1$ and $3q+2$, $q \in \mathbb{N}$), whereas the harmonics of order $3q$ are strongly suppressed since they are forbidden by symmetry [2]. This row of harmonics is always present and is designated as "undiffracted" signal ($m = 0$). When the pump pulses overlap with the bi-circular probe ($\Delta t = T_0$, panel b), a wave-mixing pattern consisting of two vertically displaced rows surrounding the main maxima is observed. The frequency and the direction of emission shows that these components result from a high-order wave mixing process [3] involving one photon from the pump pulses and are accordingly labelled as $wm = \pm 1$. Two additional rows of much weaker emission can be discerned in panel b, above and below the $wm = \pm 1$ signal. Using momentum- and frequency conservation laws, these emissions can be assigned to wave mixing involving two pump photons $wm = \pm 2$ and diffraction from the transient grating $m = \pm 1$. At positive pump probe delays ($\Delta t \gg T_0$, panel c), only the diffracted signal ($m = \pm 1$) persists. Under the conditions employed, diffraction leads to an observable signal for harmonic orders $H19 - H34$, with diffraction efficiency maximizing around $H25 - H28$ and progressively decreasing towards the cutoff region.

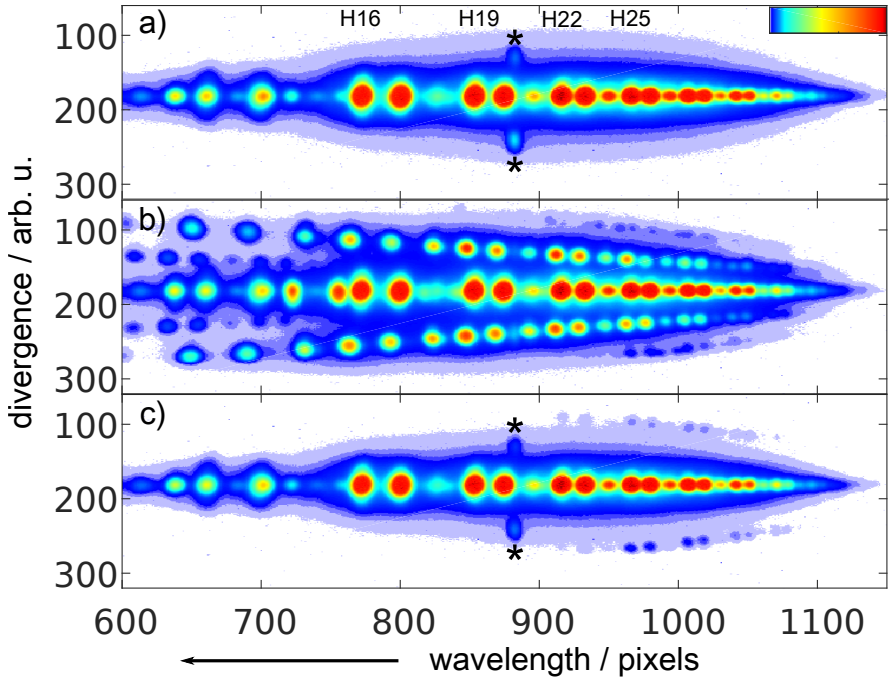

FIG. S1: Far-field high-harmonic emission profiles generated in 2-iodobutane at different pump-probe delays. The colormap (cp. upper right corner of panel a) has been saturated to improve the visibility in the diffraction peaks in panel c. Panel a: High-harmonic spectrum at negative time delays, consisting only of the undiffracted emission ($m = 0$); b: wave-mixing between 266 nm, 900 nm and 1800 nm leads to additional emissions at the position of $wm = \pm 1$ and $m = \pm 1$ spots; c: at positive time delays, after the interaction with the pump pulse has finished, only the transient grating signal in the $m = \pm 1$-diffraction orders persists. The off-axis peaks marked with black stars in panels a and c correspond to the third harmonic of the 266 nm pump (13.5 eV).

The room-temperature vapor pressure of 2-iodobutane amounts to 60 mbar at $T = 298\,\mathrm{K}$, while its (standard-pressure) boiling point lies at 391.15 K. In order to produce sufficient gas density for stable HHG, the samples were heated up to 80° C. The remaining parts of the system were kept at 100° C (pipeline) or 120° C (nozzle). The $2-C_4H_9I$-vapour was seeded in He at a stagnation pressure of ~ 1 bar. A total of ~ 0.6 mJ were available in the probe arm (~ 0.5 mJ in the 1800 nm-arm and ~ 0.1 mJ in the 900 nm arm), giving an estimate of $I_\omega \approx 5 \times 10^{13}\,\mathrm{W/cm^2}$ and $I_{2\omega} \approx 0.7 \times 10^{13}\,\mathrm{W/cm^2}$ for the laser intensities in the focus. Up to harmonic order 35 of 1800 nm could be observed (~ 24.1 eV). The synchronization between the laser pulse and the pulse of the gas delivery valve was adjusted such that the front part

of the supersonic expansion is probed in order to suppress the possible contributions from clusters.

B. Characterization of the UV-induced photodissociation dynamics of 2-iodobutane

The signal extraction procedure is based upon integration over a narrow integration window placed around each diffraction peak. As the transient-grating signal is absent prior to the arrival of the pump pulse, the intensity in the corresponding image areas at negative time delays was averaged and the resulting value was treated as a background contribution and subtracted from the signal. This procedure is applied for both diffraction orders ($m = \pm 1$) and wave-mixing signals ($wm = \pm 1$). Afterwards, the main ($m = 0$) peaks are normalized with respect to the average of the non-diffracted signal at negative time delays, and the $m = \pm 1$-transients are subsequently divided by the total signal at the given harmonic energy as a function of time, i.e. $S_{\mathrm{tot}} = I_{m=-1} + I_{m=0} + I_{m=+1}$.

The recorded transients are fitted to the following phenomenological expression(s):

$$I_{m=\pm 1}(t) = \left(c_1 \mathrm{e}^{-\frac{t-T_0}{\tau_1}} + c_2 \left(1 - \mathrm{e}^{-\frac{t-T_0}{\tau_2}} \right) + c_3 \right) \Theta(t - T_0) * g(t - T_0; \tau); \tag{1}$$

$$I_{m=0}(t) = c_3' - \left(c_1' \mathrm{e}^{-\frac{t-T_0}{\tau_1'}} + c_2' \left(1 - \mathrm{e}^{-\frac{t-T_0}{\tau_2'}} \right) \right) \Theta(t - T_0) * g(t - T_0; \tau), \tag{2}$$

with adjustable parameters c_1, c_2, c_3, τ_1 and τ_2 (as well as the corresponding primed quantities). In the above $\Theta(t)$ is the Heaviside function, and $*$ denotes the convolution with the Gaussian intensity envelope $g(t; \tau)$ of pulse width τ. In practice, the last parameter is extracted from the wave-mixing peaks and $\tau \approx 45\,\mathrm{fs}$. The time origin T_0 is set at the maximum of the wave-mixing signal. Whereas τ_1 corresponds to the rapid decay of the wave-mixing signal after the loss of the pump-probe temporal overlap, the constant $\tau_2 \equiv \tau_{\mathrm{rise}}$ models the exponential intensity build-up in the diffraction signal and as such represents a characteristic for the reaction process. The temporal profile of the undiffracted orders is given by an abrupt signal loss as the three pulses overlap followed by a rapid partial recovery. After approx. 100 fs, slow exponential decay sets in, and in the long-time limit, it converges to an asymptotic level $I_{m=0}(t \gg T_0) \ll I_{m=0}(t < T_0)$. This behaviour is qualitatively similar for

all resolved harmonic orders of 1800 nm.

Table I lists the fitted values of the build-up constant τ_{rise} for all harmonic orders for which diffraction was observed (16-35). The diffracted signal level in the "forbidden" $3q$-orders is extremely low and does not permit reliable fit results. The values in Tab. I represent an average over multiple independent measurements, whereby the signal has been averaged over both $m = +1$ and $m = -1$ orders.

Harmonic order	$\tau_{\mathrm{rise}}^{m=\pm1}$ / fs	N
16	345 ± 282	2
17	246 ± 39	2
19	234 ± 48	6
20	288 ± 48	6
22	294 ± 58	9
23	311 ± 81	7
25	341 ± 63	9
26	329 ± 54	10
28	352 ± 53	11
29	362 ± 67	7
31	348 ± 48	5
32	363 ± 49	6
34	454 ± 20	2
35	527 ± 22	2

TABLE I: Fitted values of the build-up constant τ_{rise}, statistically averaged over multiple measurements. The number of data sets considered for each harmonic order is denoted by N.

C. Evaluation of the degree of CD

The quantification of the degree of circular dichroism (CD) proceeds via evaluating the HHG intensity asymmetries between the two enantiomers as a function of the ellipticity (resp. the QWP angle α). First, the measured traces corresponding to the two enantiomers are normalized with respect to the signal integrated over the entire scanned range as a

function of the QWP angle α, i.e.

$$I_{\mathrm{R/S}}(\alpha, n\omega) = \frac{\tilde{I}_{\mathrm{R/S}}(\alpha, n\omega)}{\int_{\alpha} \tilde{I}_{\mathrm{R/S}}(\alpha, n\omega)\mathrm{d}\alpha}, \tag{3}$$

with $\tilde{I}_{\mathrm{R/S}}(\alpha, n\omega)$ being the signal prior to normalization. The value of the denominator in eq. (3) does not depend on the system's chirality.

The ellipticity-resolved CD discussed in the main text is defined as:

$$CD(n\omega, \alpha) = \frac{2\left(I_{\mathrm{R}}(n\omega, \alpha) - I_{\mathrm{S}}(n\omega, \alpha)\right)}{\max\left(I_{\mathrm{R}}(n\omega, \alpha) + I_{\mathrm{S}}(n\omega, \alpha)\right)}, \tag{4}$$

where max stands for the maximum with respect to α. Integration of this quantity over a narrow QWP-range according to Eq. (1) of the main text yields the energy-dependent CD $\overline{CD}^{\pm}(\omega)$.

II. SYNTHESIS OF 2-IODOBUTANE

The synthesis of 2-iodobutane followed the reaction scheme shown in Fig. S2. 21.2 g triphenylphosphine (81 mmol) and 16.8 g tetraiodomethane (32 mmol) were placed in a three-neck round bottom flask equipped with a dropping funnel, a magnetic stirring bar, a septum, and an empty column with a P_2O_5-filled column on top. The column was directly connected to a cooling trap filled with liquid N_2, which was connected to a vacuum line (10^{-3} mbar). The vacuum line was equipped with a three-way-valve that was connected to a balloon and a nitrogen supply (dried over P_2O_5). Through a septum, 45 ml of tetraethylenglycole dimethylether (TEG-DME) were added with the suspension turning red. The apparatus was evacuated to remove traces of air in the suspension. Under vacuum, 2 g of the respective enantiopure 2-butanol (*(R)-* or *(S)-*) was placed in the dropping funnel and added via a submerged teflon tube with the product condensing in the cooling trap. After the addition of 2-butanol was completed, a maximum of 2 hours of condensation was performed because of the observed decrease of the enantiomeric excess (*ee*) over time. In the case of *(S)*-2-iodobutane the yield was 40 % (and up to 60-65 % *ee*), and for *(R)*-2-iodobutane the yield was 57 % (and up to 60-65 % *ee*). All the analyses were performed with a GC-MS System equipped with a Lipodex C column from Macherey Nagel on which *(S)*-2-iodobutane and *(R)*-2-iodobutane have retention times of 6.7 min and 6.8 min, respectively.

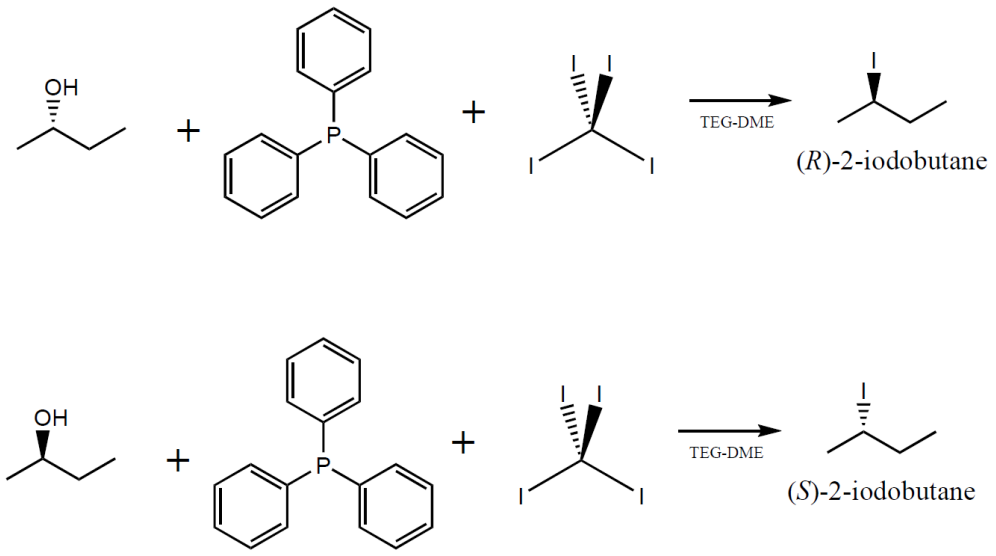

FIG. S2: Reaction scheme for the synthesis of *(R)*- and *(S)*-2-iodobutane

III. POTENTIAL ENERGY CURVES

A. Potential energy curves along the "frozen" dissociation path

The potential-energy curves required for the wavepacket propagation (s. Sec. IV) after the 266 nm-pump-excitation step were obtained with the `Molpro` program package [4]. The aug-cc-pVTZ-basis set was used for C and H, whereas the aug-cc-pVQZ-PP set was chosen for iodine. The 28 core electrons of I are approximated with the relativistic energy-consistent ECP28MDF-effective-core potential of the Stuttgart/Cologne group [5]. As a first step, the equilibrium geometry is optimized using second-order Møller-Plesset perturbation theory (MP2). The atomic coordinates at the equilibrium position are summarized in Tab. II. The potential energy (PE) curve corresponding to the cleavage of the C-I-bond (with an equilibrium distance of 2.173 Å) was obtained by varying the distance of the reaction coordinate $r_{\mathrm{C-I}}$ in the range $1.8 - 6.5$ Å and performing a single-point energy calculation at each value. The positions of the remaining coordinates have been kept fixed at their equilibrium values.

At each point of the potential energy curve, an SCF calculation is performed first, yielding the energies of the 29 orbitals in the ground state. This calculation is then followed by a state-averaged CASSCF comprising three singlet (^{1}A) and three triplet (^{3}A) states. The

Atom	x	y	z
C	-3.1586	0.2329	0.02371
C	-1.6402	0.1799	-0.02283
H	-3.4753	1.2772	0.02545
H	-3.5849	-0.2556	-0.85046
H	-3.5489	-0.2494	0.91554
H	-1.2092	0.6020	0.88332
C	-1.0663	0.8646	-1.25381
C	0.4519	0.9960	-1.25988
H	-1.5129	1.8630	-1.28130
H	-1.4109	0.3384	-2.14519
H	0.7856	1.5462	-2.13660
H	0.7940	1.5318	-0.37550
H	0.9287	0.0189	-1.27048
I	-1.0159	-1.8999	0.05212

TABLE II: Optimized geometry of *(R)*-2-iodobutane (in Ångstrom), calculated with the MP2 method and an aug-cc-pVTZ basis set for the C and H atoms. For the iodine atom, an aug-cc-pVQZ basis and an effective potential (ECP28MDF) were employed.

chosen active space is rather limited and comprises 6 electrons in 4 orbitals (6,4). A multi-reference configuration-interaction (MRCI) calculation is performed subsequently, with a reference space consisting of the CASSCF active space. These calculations are accompanied by the corresponding spin-orbit-splitting corrections.

The cationic PE-curve was obtained in the same manner, whereby the $r_{\mathrm{C-I}}$ distance was varied and all remaining degrees of freedom were fixed at the equilibrium values of the neutral species. The state-averaged active space (5,4) includes three doublet (^{2}A) and four quadruplet (^{4}A) states.

In the remaining part, when discussing the photodissociation dynamics, the emphasis will be placed on the $^3Q_1$, $^1Q_1$ and $^3Q_0^+$ states. Whereas the $^3Q_1$ and $^1Q_1$ states require an electric-dipole perpendicular transition, the $^3Q_0^+$ state is accessible via a parallel transition. Figure S3 shows the set of relevant neutral/cationic potential-energy curves. Although the correct symmetry label of all electronic states is A, in what follows, we use the classification pertaining to the $C_{3\mathrm{v}}$-PG(M) as approximated symmetry labels for clarity. The analysis

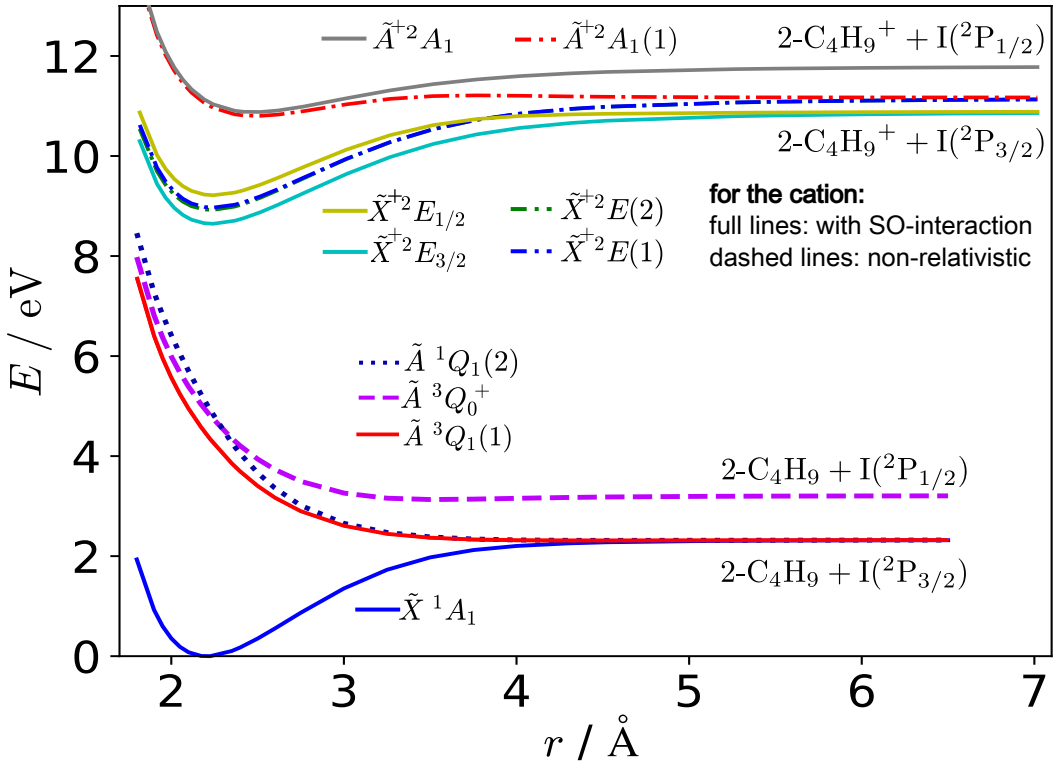

FIG. S3: Combined potential-energy curves of the neutral and the cation of 2-iodobutane as a function of the C-I distance, maintaining the other geometric parameters fixed to their value in the equilibrium geometry of the neutral ground state.

for the neutral is limited to the ground $\tilde{X}^1\mathrm{A}_1$ state and the $^3Q_1$, $^1Q_1$ and $^3Q_0^+$ excited states. At the laser intensities employed ($I_\omega \approx 5 \times 10^{13}$ W/cm^2), mainly the ground ($\tilde{X}^+$) and the first excited ($\tilde{A}^+$) states of the cation will be populated. The first two energy levels of 2-$C_4H_9I^+$ are close-to-degenerate and are designated as $\tilde{X}^+\ ^2E(1)$ and $\tilde{X}^+\ ^2E(2)$, respectively. Both belong to the dissociation limit leading to 2-$C_4H_9^+$+I^2 $P_{3/2}$ and split into two $\Omega = \frac{3}{2}, \frac{1}{2}$-components. The $\tilde{A}^+$-state correlates to 2-$C_4H_9^+$+I^2 $P_{1/2}$.

B. Potential energy curves along the "relaxed" dissociation path

In order to discriminate between the roles of the carbon-iodine bond-breaking process and the gradual planarization of the chiral environment around the radical center in the *(sec)*-butyl fragment and to obtain an estimate of the relative contributions of these processes to the chiral response, we calculate the chiral dynamics with the aid of the 2-level model described in Sec. V using potential energy curves and transition dipole moments obtained

from *(1)*: quantum chemistry calculations considering geometries where only the C-I ($r_{\mathrm{C-I}}$) distance is varied; and *(2):* QC calculations where all the remaining degrees of freedom are allowed to relax at each C-I distance. In what follows, these two sets of calculations will be referred to as "frozen" and "relaxed" scans, respectively. The calculations constituting the "fixed" dissociation pathway have been outlined in the preceding section (s. Sec. III A). The current subsection summarizes the technical details pertaining to the calculation of the "relaxed" geometries, the associated potential energy curves, and the corresponding transition dipole moments.

1. Calculation of the "relaxed" potential energy curves

In order to obtain "relaxed" structures of 2-iodobutane in the ${}^3Q_0^+$ state along the dissociation coordinate, we perform a geometry optimization procedure using the MP2 method, employing a full-electron cc-pVTZ basis set for the C and the H atoms and a cc-pVQZ-PP basis set in combination with the relativistically corrected SK-MCDHF-RSC-pseudopotential [5] for the iodine atom. The distance between the secondary carbon and the iodine is fixed at each step, whereas the coordinates of the remaining atoms are allowed to vary.

On the basis of this new structural information, potential energy surfaces along the "relaxed" dissociation path were calculated for the $\tilde{A}\ {}^3Q_0^+$ excited state of the neutral as well as for the ground- and excited states of the cation. Thereby, the quasi-degenerate second-order N-electron valence state perturbation (QD-NEVPT2) method was used as implemented in the program package `ORCA` [6]. The resulting curves are shown as dashed lines in Figs. S4 (neutral) resp. S5 (cation). The calculations employed the aug-cc-pVTZ-DK basis for C and H and the (all-electron) aug-cc-pVQZ-DK basis for iodine, and considered three singlet / three triplet states as a reference space for the neutral molecule resp. three doublet / three quadruplet states for the cation. In Figs. S4 and S5, we compare the PES along the "relaxed path" with analogous calculations employing the "fixed" geometries for the states that are relevant for the 2-level ODE model (s. Sec. V), i.e. the ${}^3Q_0^+$ state of the neutral as well as the two lowest states of the cation (denoted as $\tilde{X}^+$ and $\tilde{A}^+$, respectively). The cationic curves were calculated under the assumption that the geometry does not change upon ionization, which is a reasonable approximation given the short durations of the electron trajecto-

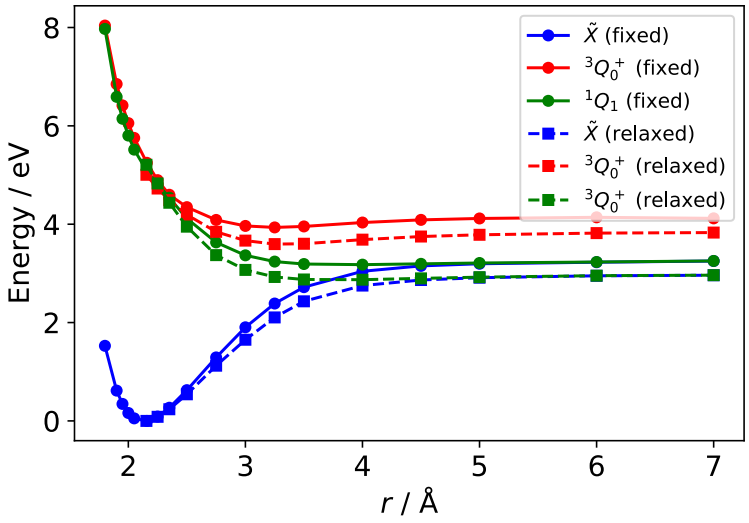

FIG. S4: Potential energy curves of the neutral 2-iodobutane as a function of the C-I distance calculated with all remaining degrees of freedom kept fixed to their equilibrium values (full lines), and after optimizing the remaining coordinates at each $r_{\mathrm{C-I}}$-step (dashed lines).

ries (1-3 fs). Figures S4 and S5 imply that whereas relaxing the geometry has relatively little effect on the neutral PES, it has a significantly larger influence in the case of the cation.

The modifications of the PES along the dissociation path essentially imply a modification of the effective ionization potentials associated with the two considered cationic states, which has an effect on the length of the electron continuum trajectories (τ). The latter determine the propagation time in the solution of the 2-level dynamics. These changes have been taken into account in our "relaxed" model. Overall, relaxing the geometry leads to an increased duration of the continuum trajectory. It should be noted that for the "relaxed" CD calculations reported in main text, a distance-to-time mapping derived from the wavepacket calculation in Section IV has been used.

2. Transition dipole matrix elements as a function of the bond distance

One of the key quantities determining the temporal behavior of the chiral response is the variation of the electric- and the magnetic-dipole transition matrix elements ($\hat{\mu}$ and $\hat{m}$) relating the ground- and the excited states of the cation as a function of the C-I bond

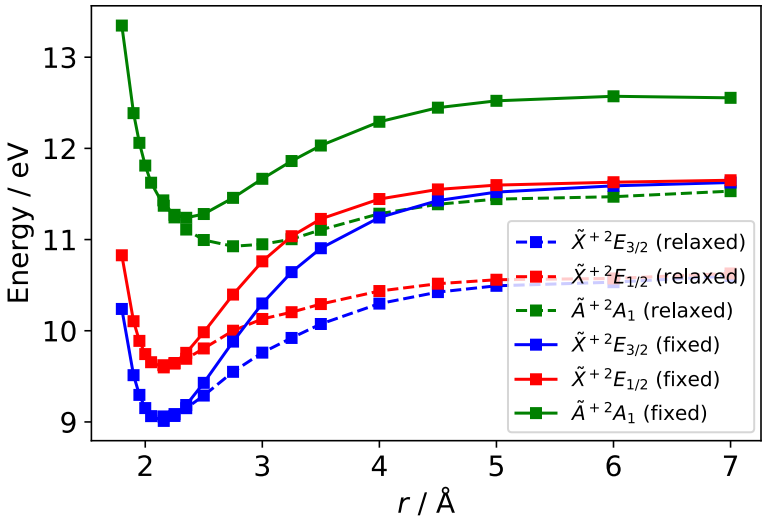

FIG. S5: Selected potential energy curves of the 2-iodobutane cation as a function of the C-I distance calculated with all remaining degrees of freedom kept fixed to their equilibrium values (full lines), and after optimizing the remaining coordinates at each $r_{\mathrm{C-I}}$-step (dashed lines).

distance. These quantities have been calculated with the methods described in the preceding sections III A and III B 1. Figure S13 displays the variation of the electric and the magnetic transition dipole moment for the "frozen" dissociation path separately. Figures S6 and S7 compare the absolute magnitudes as well as the individual Cartesian components of $\hat{\mu}$ and $\hat{m}$ in the "relaxed" vs. the "fixed"-geometry dissociation paths. Generally, the qualitative behavior of the two sets of results is similar.

In the actual implementation of our 2-level model, we consider only 2-iodobutane molecules with a C-I-bond aligned parallel to the laser field due to the selective excitation induced by the UV-excitation pulse as explained in one of the following sections (cp. Section VI of the SM). Therefore, it is the projection of the above transition dipoles on the C-I-bond-vector that essentially governs the dynamics. Figures S8 a and b display the projected electric and magnetic transition dipoles in the "fixed" vs. the "relaxed" cases. As before, the qualitative behavior is very similar. The magnetic dipole exhibits a deviation in terms of the absolute value, however, the variation as a function of the C-I-bond distance is very similar. We emphasize that our model is aimed at explaining the temporal variation of the chiral response, which is to a substantial extent dictated by the variation of the $\hat{\mu}$ /

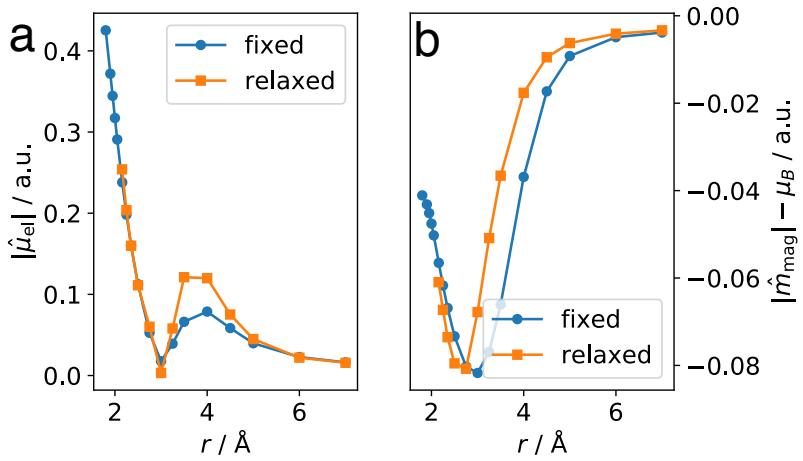

FIG. S6: Absolute magnitudes of the electric (panel a) and the magnetic (panel b) transition-dipole moments between the ground ($\tilde{X}^+$) and the first excited ($\tilde{A}^+$) states of the 2-iodobutane cation as a function of the C-I distance, obtained from an all-electron QD-NEVPT2-calculation employing the Douglas-Kroll-Hess method along the "fixed" and the "relaxed" dissociation paths.

$\hat{m}$ as a function of $r_{\mathrm{C-I}}$, and not at the absolute value of the chiral effect. Further, we note that the dipole moment expectation values for the "relaxed" geometry entering Eq. 5 are taken from a MRCI calculation similar to the one described in Sec. III A.

3. Dynamics of the chiral response in the case of the "frozen" dissociation pathway

As a final step, we combine the results outlined in the above sections and calculate the time-dependent chiral response according to the model described in the main text and elaborated in Sec. V of the SM. The results obtained with the "relaxed" geometries are presented in Fig. 5 of the main text, whereas the chiral dynamics for harmonic orders 16, 20, and 31, calculated assuming a "frozen" dissociation path, are presented in Fig. S9 of the current text.

Apart from the short-time region, the predicted chiral response decay in the "fixed-geometry"-case takes place on a time scale, which is almost identical to the previous theoretical results and also similar to the experimental results (250-300 fs). From the plots displaying the variation of the magnitude of the magnetic moment as a function of distance,

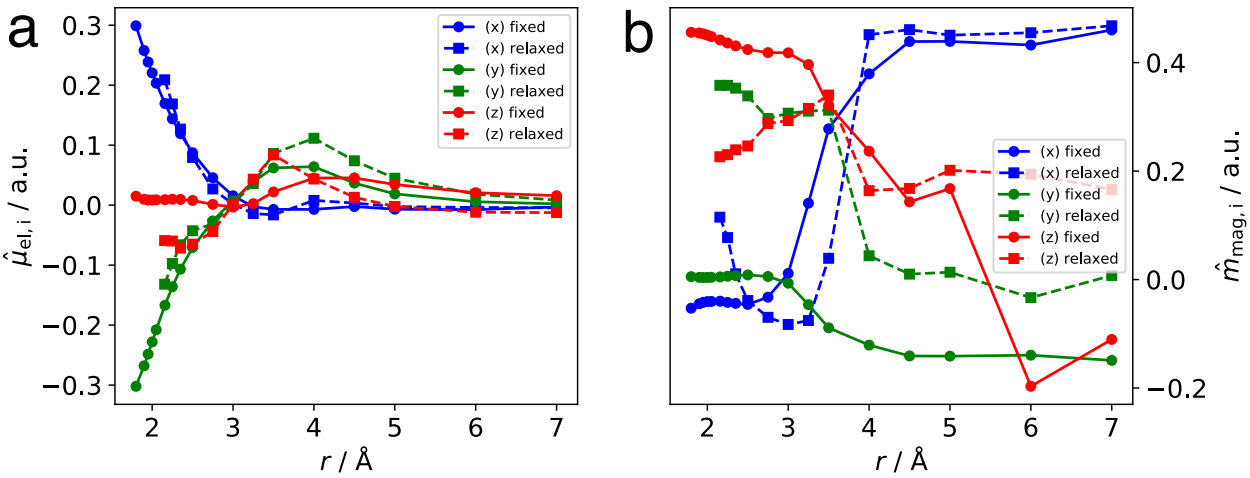

FIG. S7: Molecular-frame components of the electric (panel a) and the magnetic (panel b) transition-dipole moments between the ground ($\tilde{X}^+$) and the first excited ($\tilde{A}^+$) states of the 2-iodobutane cation as a function of the C-I distance, obtained from an all-electron QD-NEVPT2-calculation employing the Douglas-Kroll-Hess method along the "fixed" and the "relaxed" dissociation paths.

one can infer that relaxing the nuclear framework leads to a slightly faster decay to the atomic value (i.e. the Bohr magneton μ_{B}, which has been subtracted in all figures presented in the current text). However, this effect seems to be counter-balanced by the fact that the electron transit time is increased in the relaxed case, which leads to a more efficient population transfer between the $\tilde{X}^+$ and the $\tilde{A}^+$ states.

Therefore, we conclude that the relaxation of the geometry of the 2-butyl fragment does not significantly influence the predicted chiral dynamics. Consequently, the primary aspect of the chiral dynamics probed by our experiment is not the planarization of the 2-butyl radical, but instead the separation of the iodine atom from the 2-butyl radical.

IV. WAVEPACKET CALCULATIONS

The photodissociation dynamics are modelled by propagating the nuclear wavepacket on the repulsive $^3Q_0^+$ and $^1Q_1$ states of 2-iodobutane using the potential energy surfaces described in the preceding section (cp. also Fig. S3). Only the coupling between the ground state and each of the excited states is taken into account and the corresponding transition

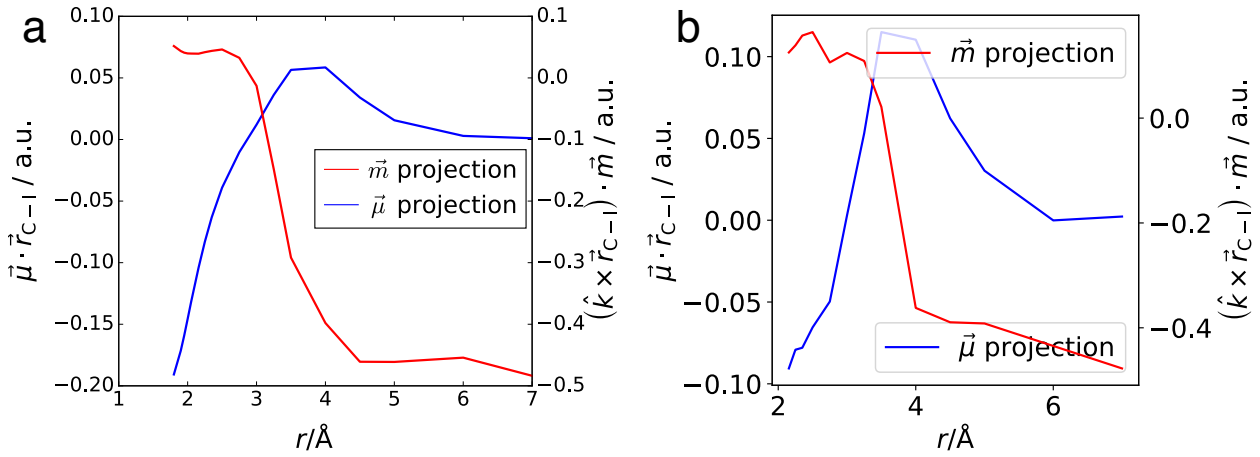

FIG. S8: Projections of the molecular-frame components of the electric (blue) and the magnetic (red) transition-dipole moments between the ground ($\tilde{X}^+$) and the first excited ($\tilde{A}^+$) states of the 2-iodobutane cation onto the C-I-bond vector as a function of the C-I distance, obtained from an all-electron QD-NEVPT2-calculation employing the Douglas-Kroll-Hess method along the "fixed" (panel a) and the "relaxed" (panel b) dissociation paths.

dipole moments are displayed in Fig. S10. These curves were obtained with `Molpro` [4] (using the MRCI method and the parameters described above).

The pump direction is set parallel to the C-I-bond (cp. Fig. S11). The time-dependent Schrödinger equation (in one dimension) is solved with the split-operator method coupled with the fast-Fourier transform technique. The time step was $\Delta t = 0.05$ fs and the spatial grid representing the r_{C-I}-reaction coordinate consisted of 2^{13} points extending from 1.8 Å to 45 Å. The excitation pulse was modelled by a Gaussian pulse with a duration of 45 fs and an intensity of 4×10^{12} W/cm^2. An absorbing imaginary potential was employed in order to prevent reflection from the grid boundary. Figure S12 shows the calculated time evolution of the expectation value of the C-I-distance in each of the two excited states. Assuming that the infinite-separation limit is effectively reached at $r_{C-I} > 8$Å, the dissociation process can be considered as completed after ≈ 160 fs.

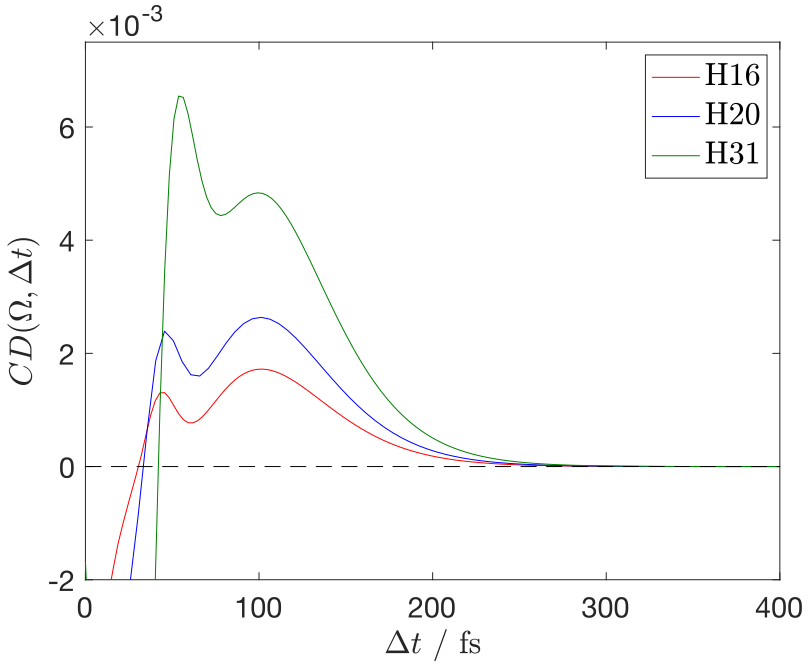

FIG. S9: Time-dependent chiral resonse, evaluated according to the methods presented in Sec. V assuming a "frozen" dissociation path for harmonic orders 16, 20 an 31 of 1800 nm.

V. TWO-LEVEL MODEL OF THE LASER-INDUCED DYNAMICS IN THE 2-IODOBUTANE CATION

Following the treatment presented in Refs. [7–10], the 2-level ordinary-differential-equation (ODE) system is given by:

$$i\partial_t \boldsymbol{c_{IJ}} = \begin{pmatrix} E_{\tilde{X}^+}(t) & 0 \\ 0 & E_{\tilde{A}^+}(t) \end{pmatrix} \cdot \boldsymbol{c_{IJ}} + \begin{pmatrix} V_{XX}(t) & V_{XA}(t) \\ V_{AX}(t) & V_{AA}(t) \end{pmatrix} \cdot \boldsymbol{c_{IJ}}, \tag{5}$$

where $\boldsymbol{c_{IJ}}(t)$ is the coefficient vector corresponding to ionization into the cationic state I and recombination with the state J. $E_{\tilde{I}^+}$ are the corresponding eigenenergies, whereby the influence of the spin-orbit interaction has been neglected. The initial conditions read:

$$\boldsymbol{c_X} = \begin{pmatrix} 1 \\ 0 \end{pmatrix} \quad \text{for} \quad I = X \quad \text{and} \quad \boldsymbol{c_A} = \begin{pmatrix} 0 \\ 1 \end{pmatrix} \quad \text{for} \quad I = A. \tag{6}$$

In the above, $V_{IJ}(t) = \langle J | \hat{H}_{\text{int}}(t) | I \rangle$. Thus, V_{XX} and V_{AA} are the dipole-moment expectation values of the two states, and the cross terms correspond to the transition moments which are related to the electric (ETDM) and the magnetic (MTDM) transition dipole moments

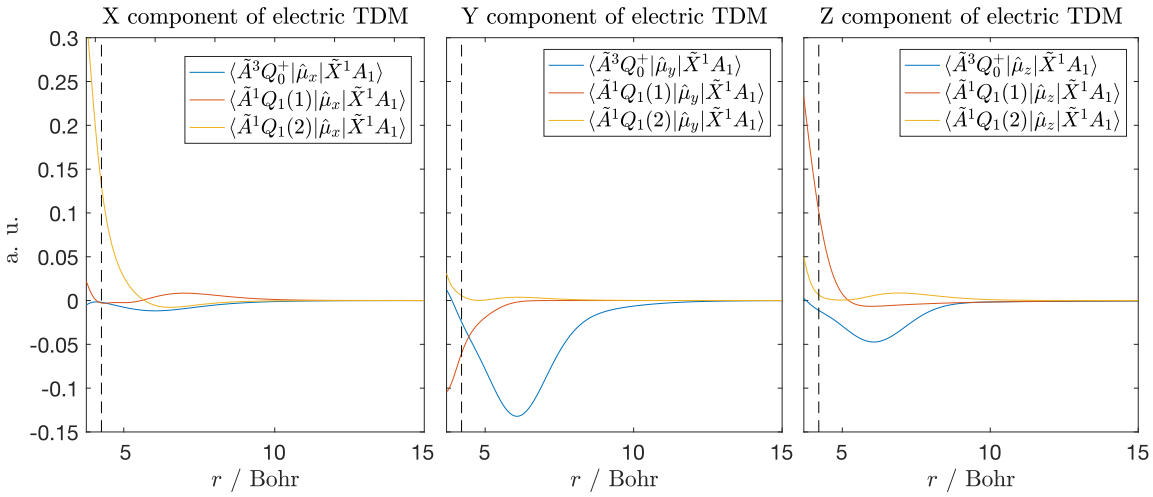

FIG. S10: Components of the electric transition-dipole moments from the ground state to each of the two excited states of neutral 2-iodobutane considered in the model, as a function of the C-I distance. The equilibrium C-I distance is indicated as a dashed vertical line.

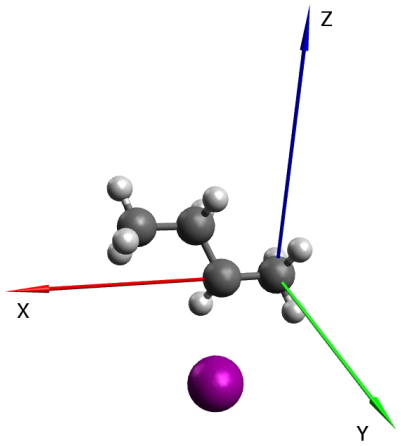

FIG. S11: Definition of the molecule-fixed (Cartesian) coordinate system. In the main text, a "parallel" transition is defined by the transition dipole being parallel to the C-I-bond. In the graphic, the length of the dissociating C-I-bond is set to 5 Å.

as:

$$V_{XA} = V_{XA}^{(\mathrm{el})} + V_{XA}^{(\mathrm{mag})}$$
$$V_{AX} = V_{AX}^{(\mathrm{el})} + V_{AX}^{(\mathrm{mag})} = V_{XA}^{(\mathrm{el})} - V_{XA}^{(\mathrm{mag})}. \quad (7)$$

The coupling matrix elements were obtained from an all-electron calculation employing

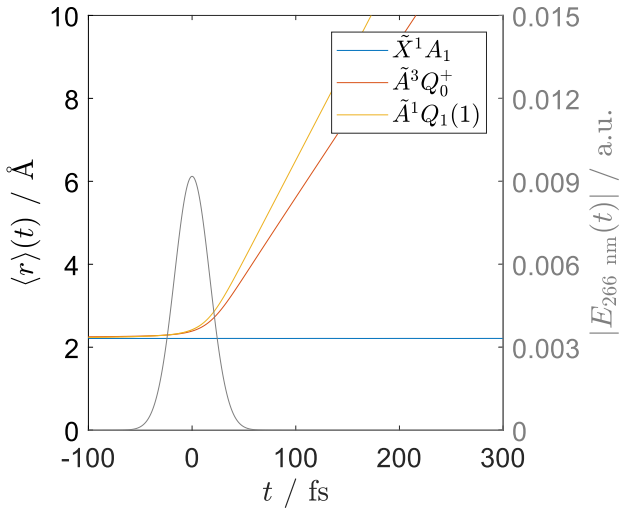

FIG. S12: Expectation value of the iodine-2-butyl separation as a function of time, evaluated over each of the three potential energy surfaces considered in the main text. The electric-field envelope with a FWHM duration of 45 fs is shown in grey.

the quasi-degenerate second-order N-electron valence state perturbation theory approach as implemented in the software package `Orca` [6]. We used the aug-cc-pVTZ-DK basis for C and H and the (all-electron) aug-cc-pVQZ-DK basis for iodine. To our knowledge, `Orca` does not support calculations of the magnetic component of the transition dipole moment that take relativistic interactions into account. For this reason, the spin-orbit splitting of the considered cationic states has been neglected.

The interaction Hamiltonian is:

$$\hat{H}_{\mathrm{int}} = -\boldsymbol{F}(t) \cdot \hat{\boldsymbol{\mu}} - \boldsymbol{B}(t) \cdot \hat{\boldsymbol{m}} = -\boldsymbol{F}(t) \cdot \hat{\boldsymbol{\mu}} - \frac{1}{c} \left(\hat{\boldsymbol{k}} \times \boldsymbol{F}(t) \right) \cdot \hat{\boldsymbol{m}}. \tag{8}$$

Thereby, $\boldsymbol{F}(t)$ denotes the electric component of the bi-circular field:

$$\boldsymbol{F}(t) = F_0 \begin{pmatrix} \cos(\omega t) + \eta \cos(2\omega t) \\ \sin(\omega t) - \eta \sin(2\omega t) \end{pmatrix}, \tag{9}$$

with η being the ratio of the field strengths of the fundamental and the second harmonic and $\hat{\boldsymbol{k}}$ the propagation direction of the bi-circular field. $\boldsymbol{B}(t)$ is the magnetic-field component, and we consider one full cycle of the fundamental field in the cw-limit. We consider only ionization events, whereby the instantaneous polarization axis of $\boldsymbol{F}(t)$ points along the C-I bond, and average over all possible azimuthal directions. According to quantum-orbit analysis, typical electron excursion times (τ) under the present experimental conditions

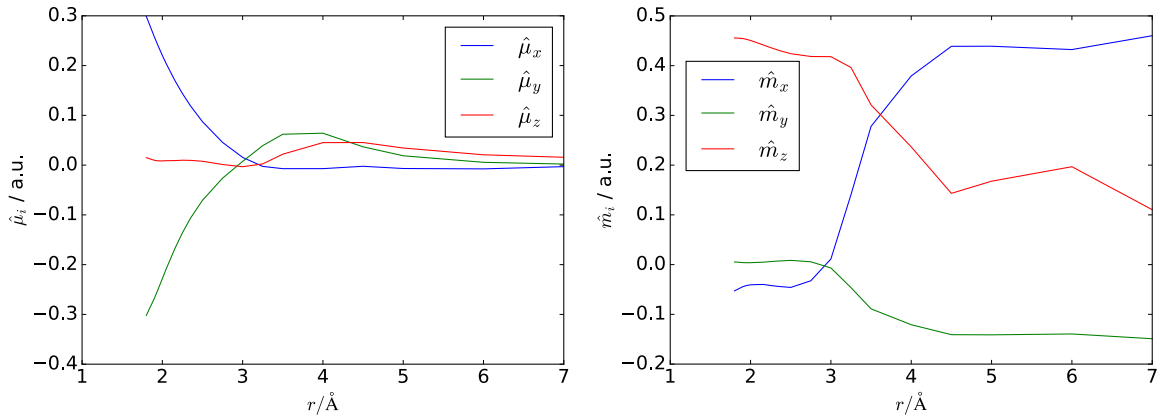

(a) Electric TDM.

(b) Magnetic TDM.

FIG. S13: Components (in the molecular frame) of the electric and the magnetic transition-dipole moments between the ground ($\tilde{X}^+$) and the first excited states of the 2-iodobutane cation as a function of the C-I distance, obtained from an all-electron QD-NEVPT2-calculation employing the Douglas-Kroll-Hess method. The TDMs shown do not include the SO-correction.

range from 1.4 to 1.8 fs. The ODE in Eq. (5) is thus propagated from an initial value of the pump-probe delay Δt to the instant of recombination $\Delta t + \overline{\tau}^{\Omega}_{IJ}$. The time dependence of the potential energy curves and the matrix elements is estimated on the basis of the quantum-mechanical calculations presented in Section III and the wavepacket analysis (s. Section IV) using a classical trajectory treatment. Since one of the dissociation fragments is an iodine atom in its spin-doublet ground state, the magnetic transition dipole at asymptotic distances is dominated by the transition between the two Kramers-degenerate magnetic sub-components, yielding an artificial contribution to the calculated chiral response. This contribution has therefore been subtracted from the value obtained with Eq. (3) of the main text.

VI. PUMP-INDUCED ROTATIONAL ANISOTROPY

In order to estimate the extent to which the rotational anisotropy induced by the 266 nm-pump pulse influences the temporal profile of the chiral response, a calculation of the time evolution of the initially created rotational alignment was performed. Two of the rotational constants of 2-iodobutane (B and C), which itself belongs to the class of asymmetric rotors,

A / GHz	B / GHz	C / GHz
3.755	1.709	1.236
I_a / (kg m^2)	I_b / (kg m^2)	I_c / (kg m^2)
$2.235 \cdot 10^{-45}$	$4.910 \cdot 10^{-45}$	$6.788 \cdot 10^{-45}$

TABLE III: Rotational constants and moments of inertia of 2-iodobutane.

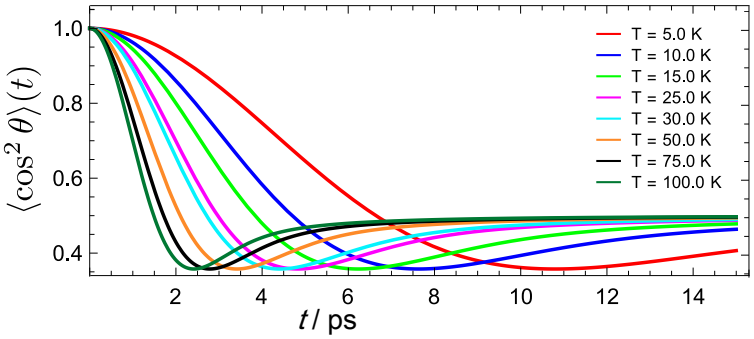

FIG. S14: Time evolution of the rotational anisotropy of neutral 2-iodobutane calculated with the aid of Eq. (10) and the parameters described in the text for a range of rotational temperatures. The anisotropy is quantified in terms of the expectation value of the degree of alignment ($\langle\cos^2\vartheta\rangle$) with respect to the laser polarization axis.

are comparable, enabling one to treat the molecule in the symmetric-top approximation. For this aim, the B- and the C- constants were averaged. This simplification enables one to make use of the theoretical framework for symmetric-top systems that was recently developed in Refs. [11] and [12]. According to Eq. (4) in Ref. [12], the rotational distribution of excited-state molecules is given by

$$\left\langle\cos^2\vartheta\right\rangle(t) \equiv \left\langle\cos^2\omega t\right\rangle = \int_0^\infty 2a\omega \mathrm{e}^{-a\omega^2}\cos^2(\omega t)\,\mathrm{d}\omega \tag{10}$$

for an initially randomly oriented ensemble and single-photon pump-probe processes. In the above, ϑ denotes the angle between the polarization vector of the pump beam and the transition dipole moment of the molecule and $a = \frac{J_1}{2k_\mathrm{B}T}\xi^2$, whereby $\xi = \left(\frac{1}{3}(2+\chi^{-1})\right)^{-1/2}$ and $\chi = J_3/J_1 (\chi \in [\frac{1}{2}, \infty])$. For the (quasi)-symmetric-top molecule under consideration, the quantities J_1 and J_3 correspond to the moments of inertia in the principal axis system: $J_1 = I_b$ and $J_3 = I_a$. The rotational constants and the moments of inertia of the 2-iodobutane molecule obtained after the geometry optimization step are reported in Tab. III. With these approximations, the calculated temporal evolution of the initially created transient rotational

distribution in the excited state is plotted in Fig. S14 for a range of rotational temperatures.

VII. BARRIERS FOR THE INTERCONVERSION OF THE CONFORMERS OF THE 2-BUTYL RADICAL

Despite being one of the structurally simplest chiral alkyl radicals, to date, both experimental and theoretical studies of the 2-butyl radical have remained scarce. Due to the steric hindrance exerted by the methyl and the ethyl substituents, the local arrangement around the α-carbon atom is no longer planar (as in the case of the methyl radical), and the resulting pyramidal ("tripodal") arrangement of the bonds creates a chiral environment. A theoretical study [13] of the structure and the rotational barriers of the 2-butyl radical employing unrestricted Hartree-Fock theory with the 6-31G*-basis set predicts a total of six equilibrium structures in its electronic ground state, which can be grouped into three pairs of enantiomeric conformations. These are depicted as insets in Fig. S15. In all of them, the out-of-plane bending angle around the radical center is $\approx 20°$. One of the pairs $(3, 3')$ has no isolated existence because of the low rotational barrier separating it from the conformer pair $(2, 2')$. Of main interest for the dissociation dynamics studied in the present work is the (relaxed) potential energy curve associated with the variation of the torsional angle δ_2 along the $C^2C^3C^4$ bonds, reproduced in Fig. S15. The rotation associated with the angle δ_2 is indicated in the inset on the right-hand side of Fig. S15. Variation of δ_2 connects two twisted carbon chains possessing P- ($0 \leq \delta_2 < 180°$) or M- ($180° \leq \delta_2 < 360°$) axial chirality. As δ_2 is varied, the radical center undergoes multiple inversions of the chiral conformation. The stereomutation that interchanges the two chiral enantiomers belonging to the ground-state conformation takes place via a transition-state structure with C_s-symmetry. The barrier of this pyramidal inversion is $E_{barr} \approx 0.35$ kcal/mol. As the zero-point vibrational energy E_{ZP} of the chiral conformers $(1, 1')$ exceeds the energy of the C_s structure, it is expected that rapid racemization of the initially chiral 2-butyl radical as produced by the dissociation of 2-iodobutane will take place. Therefore, the reaction product can be expected to behave as an achiral molecule. A more rigorous analysis of this aspect is presented in the next section.

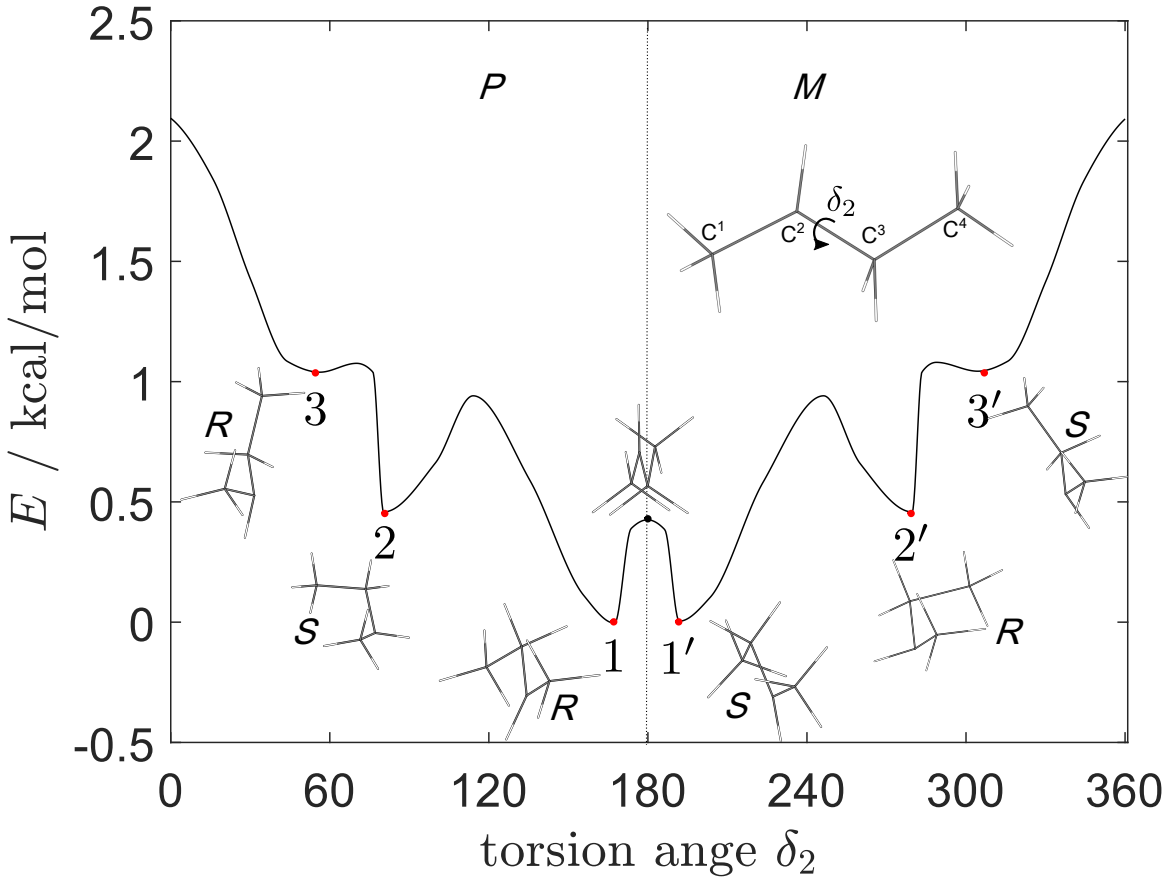

FIG. S15: Relaxed potential energy curve of the 2-butyl radical for the rotation about the torsion angle δ_2, reproduced from Ref. [13]. The dotted line indicates the inversion of the handedness of the carbon chain ($P \leftrightarrow M$) around 180°. The energies of the individual equilibrium structures (displayed in the insets) are indicated by red circles. The energy of the C_s-symmetric transition structure interconverting isomers 1 and 1′ is denoted by the black dot. The absolute (R/S)-configuration of all six structures is specified as a separate label. The inset structure in the right-top part of the figure shows the rotation associated with variation of the dihedral angle δ_2, defined by the atom chain $C^1C^2C^3C^4$.

VIII. LARGE-AMPLITUDE INTERNAL MOTION IN THE 2-BUTYL RADICAL

The photodissociation of the carbon-iodine bond in 2-iodobutane leads to the formation of the 2-butyl radical, whereby the non-planar configuration of the atom groups around the radical center C^2 renders the initial product chiral. One enantiomeric conformer is converted to the other via a large-amplitude internal motion. The aim of the current section

is to estimate the time scale of this motion in order to evaluate the implication of the racemization dynamics on the observed degree of circular dichroism in the course of the dissociation process.

In our analysis, the large-amplitude dynamics is conveyed by the variation of the dihedral angle φ_{D}, defined as the angle formed by the $\mathrm{C}^2 - \mathrm{H}$-bond and the plane defined by the C^3-, C^4-, and H^4-atoms, whereby H^4 is one of the three equivalent H-atoms belonging to the terminating methyl group (cp. Fig. S16 a). Further, this torsional mode is assumed to be separable from the remaining degrees of freedom, which are treated as frozen during the interconversion process. Following the procedure developed by Meyer and Günthard (cp. Ref. [14]), we arrive at the following one-dimensional effective Hamiltonian:

$$\hat{H}^{\mathcal{I}}(\varphi_{\mathrm{D}}) = -\frac{\hbar^2}{2}\frac{1}{m_{\mathrm{H}} r_{\mathrm{H}}^2 \sin^2(\beta_{\mathrm{H}})}\frac{\mathrm{d}^2}{\mathrm{d}\varphi_{\mathrm{D}}^2} + V^{\mathcal{I}}(\varphi_{\mathrm{D}}). \tag{11}$$

In the above, m_{H} denotes the mass of the H-atom, r_{H} is the $\mathrm{H} - \mathrm{C}^2$ bond distance, and $\beta_{\mathrm{H}} = \pi - \alpha_{\mathrm{H}}$ where α_{H} stands for the angle between the "active" H-atom on C^2 and the $\mathrm{C}^2 - \mathrm{C}^3$-axis (cp. Fig. S16 a). $V^{\mathcal{I}}(\varphi_{\mathrm{D}})$ is the effective torsional potential, which we discuss in the following.

The effective one-dimensional torsional potential $V^{\mathcal{I}}(\varphi_{\mathrm{D}})$ is obtained by performing a relaxed potential energy scan by varying the dihedral angle φ_{D} and optimizing the geometry of the 2-butyl radical at each point using unrestricted second-order Møller-Plesset perturbation theory (UMP2) and the cc-pVTZ basis set. The equilibrium geometry obtained with this method is reported in terms of Cartesian coordinates in Tab. IV. The values along the resulting potential energy curves are shown as black circles in Fig. S16 b and the curve $V^{\mathcal{I}}(\varphi_{\mathrm{D}})$ has been shifted such that the origin of the ordinate (energy) dimension is located at the maximum of the potential barrier. These results do not include the contribution of the zero-point energy associated with the remaining $3N - 7$ active vibrational modes. The equilibrium value of φ_{D} amounts to $\varphi_{\mathrm{D}}^{\mathrm{eq}} = 27.64°$ and the height of the barrier separating the two enantiomeric conformers is $V_{\mathrm{b}}^{\mathcal{I}} = 56.84\ \mathrm{cm}^{-1}$. The zero-point vibrational energy of the corresponding mode is $E_{\mathrm{ZPE}}^{\varphi_{\mathrm{D}}}/hc = 34.89\ \mathrm{cm}^{-1}$.

The calculated one-dimensional potential in which the torsional motion takes place is

then approximated by an analytical expression of the form:

$$V^{\mathcal{I}}(\varphi_{\mathrm{D}}) = 2b\varphi_{\mathrm{D}}^2 + \sum_{l=1}^{2} c_l \left(\mathrm{e}^{-4\alpha_l \varphi_{\mathrm{D}}^2} - 1 \right) + d, \tag{12}$$

whereby the constants b, $\{c_l\}$, $\{\alpha_l\}$, and d are determined via a non-linear least-squares-fitting procedure. The fitted values are reported in Tab. V.

Atom	x	y	z
C	1.9719	0.0451	0.0563
C	0.5725	-0.4522	-0.0221
C	-0.5640	0.5065	-0.0822
C	-1.9236	-0.1650	0.0707
H	2.0699	0.8233	0.8148
H	2.6753	-0.7506	0.2920
H	2.2942	0.4929	-0.8914
H	0.3955	-1.4726	-0.3331
H	-0.5370	1.0541	-1.0347
H	-0.4337	1.2701	0.6900
H	-2.7349	0.5581	0.0108
H	-2.0759	-0.9054	-0.7137
H	-1.9942	-0.6762	1.0293

TABLE IV: Optimized geometry (UMP2/cc-pVTZ) of the 2-butyl radical in Cartesian coordinates. All distances are given in Ångstroms.

The resulting "effective" Schrödinger equation, namely:

$$\hat{H}^{\mathcal{I}}(\varphi_{\mathrm{D}}) = -\frac{\hbar^2}{2} \frac{1}{m_{\mathrm{H}} r_{\mathrm{H}}^2 \sin^2(\beta_{\mathrm{H}})} \frac{\mathrm{d}^2}{\mathrm{d}\varphi_{\mathrm{D}}^2} + 2b\varphi_{\mathrm{D}}^2 + \sum_{l=1}^{2} c_l (\mathrm{e}^{-4\alpha_l \varphi_{\mathrm{D}}^2} - 1) + d \tag{13}$$

is then solved using the discrete-variable representation (DVR) method as implemented by Colbert and Miller [15]. Thereby, a grid consisting of 5001 points spanning the range $\varphi_{\mathrm{D}} \in [-60°, 60°]$ is employed. Table VI lists the eigenvalues of the first six levels supported by $V^{\mathcal{I}}(\varphi_{\mathrm{D}})$, referenced to the maximum of the potential energy barrier ($V_{\mathrm{b}}^{\mathcal{I}}(\varphi_{\mathrm{D}})$). The lowest level ($E_0^{\mathcal{I}}$) lies 12.40 cm^{-1} above the barrier. Three of these eigenlevels and the associated vibrational eigenfunctions are indicated in Fig. S16 b.

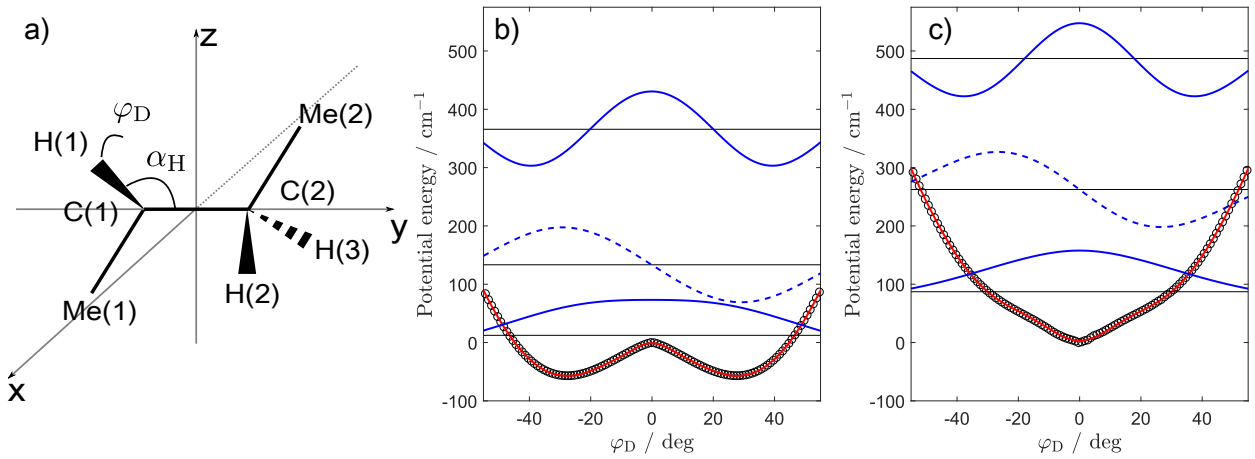

FIG. S16: Panel a: Schematic structure of 2-iodobutane used for the treatment of the large-amplitude motion. Panels b and c: Potential energy curves for the torsional motion associated with the dihedral angle φ_D calculated with the UMP2/cc-pVTZ method (black circles). The model potentials obtained by fitting Eq. (12) to these values are shown as red curves. Panel a: potential energy curve without ZPE correction. Panel b: potential energy curve including the ZPE contribution. The eigenvalues and the eigenfunctions associated with the first three levels of torsional potential are given as black and blue lines, respectively. The full/dashed curves denote the parity of the level (positive/negative).

As a further step, the influence of the zero-point vibrational motion was estimated by calculating the zero-point energy (ZPE) E_{ZPE} contribution associated with the remaining $3N-7$ vibrational modes. The ZPE-corrected potential energy curve $V^{\mathcal{I}}_{\mathrm{ZPE}}(\varphi_D)$ is shown next to the uncorrected one in panel c of Fig. S16, together with the first three energy eigenvalues and the associated eigenfunctions. The fit parameters, obtained from fitting $V^{\mathcal{I}}_{\mathrm{ZPE}}(\varphi_D)$ to the expression in Eq. (12), are presented in the two rightmost columns of Tab. V, whereas the energies of the lowest six levels are given in the bottom row of Tab. VI. The ZPE-correction leads to the disappearance of the double-minimum structure observed in $V^{\mathcal{I}}(\varphi_D)$. Instead, $V^{\mathcal{I}}_{\mathrm{ZPE}}(\varphi_D)$ is characterized by a single minimum located at $\varphi_D = 0°$.

The energy separation between the lowest two states of the one-dimensional potential $V^{\mathcal{I}}(\varphi_D)$ is 120.96 cm^{-1}, which corresponds to a beating period τ_{per} of $\approx$ 275.8 fs. If photodissociation creates a coherent superposition of these two states, the stereomutation from one enantiomer to the other would proceed in $\tau_{\mathrm{per}}/2 \approx 137.9$ fs. Including the zero-point-energy contribution increases the energy separation to 175.29 cm^{-1}, or $\tau_{\mathrm{per}} \approx 190.3$ fs. This

$V^{\mathcal{I}}(\varphi_{\mathrm{D}})$		$V^{\mathcal{I}}_{\mathrm{ZPE}}(\varphi_{\mathrm{D}})$	
Parameter	Fit result	Parameter	Fit result
$b/\mathrm{cm}^{-1}\mathrm{deg}^{-2}$	0.05328(18)	$b/\mathrm{cm}^{-1}\mathrm{deg}^{-2}$	0.0548(4)
c_1/cm^{-1}	228.9(12)	c_1/cm^{-1}	108(13)
$\alpha_1/\mathrm{deg}^{-2}$	0.0002580(20)	$\alpha_1/\mathrm{deg}^{-2}$	0.00042(5)
c_2/cm^{-1}	12.7(3)	c_2/cm^{-1}	-71(15)
$\alpha_2/\mathrm{deg}^{-2}$	0.00463(24)	$\alpha_2/\mathrm{deg}^{-2}$	0.00117(12)
d/cm^{-1}	-1.00(17)	d/cm^{-1}	3.2(3)
RMSE	$1.892 \cdot 10^{-6}$	RMSE	$4.834 \cdot 10^{-6}$

TABLE V: Parameters for the torsional model potential $V^{\mathcal{I}}(\varphi_{\mathrm{D}})$ (left) or $V^{\mathcal{I}}_{\mathrm{ZPE}}(\varphi_{\mathrm{D}})$ (right) obtained from a non-linear least-squares fit of expression (12) to the potential energy curve along the dihedral angle φ_{D} calculated with the UMP2/cc-pVTZ method. The parameter RMSE represents the root-mean square error of the fit.

Level	$E^{\mathcal{I}}_0$	$E^{\mathcal{I}}_1$	$E^{\mathcal{I}}_2$	$E^{\mathcal{I}}_3$	$E^{\mathcal{I}}_4$	$E^{\mathcal{I}}_5$
Eigenvalue / cm^{-1}	12.40	133.36	365.74	664.01	1048.50	1514.24
Eigenvalue (incl. ZPE) / cm^{-1}	87.14	262.45	487.03	792.76	1174.61	1641.34

TABLE VI: Energies corresponding to the first six eigenvalues of the torsional Hamiltonian given in Eq. (13). For $V^{\mathcal{I}}(\varphi_{\mathrm{D}})$, the values are referenced with respect to the maximum of the potential energy barrier, whereas in the case of $V^{\mathcal{I}}_{\mathrm{ZPE}}(\varphi_{\mathrm{D}})$, the reference is set at the minimum of the potential. The bottom row contains the results obtained after taking into account the zero-point-energy contribution.

value of τ_{per} is significantly smaller than the duration of the photodissociation dynamics as estimated from the time constants of the diffraction signal transients ($\sim$ 340 fs). This fact, together with the single-minimum structure of the ZPE-corrected potential $V^{\mathcal{I}}_{\mathrm{ZPE}}(\varphi_{\mathrm{D}})$ with an equilibrium position given by a planar local geometry at the C^2-atom, imply that the initially formed chiral 2-butyl conformer will be quickly converted to a racemic structure in the course of the photodissociation reaction, i.e. the absence of coherent stereomutation, which is consistent with the experimental results.

[1] O. Kfir, E. Bordo, G. Ilan Haham, O. Lahav, A. Fleischer, and O. Cohen, Applied Physics Letters **108**, 211106 (2016).

[2] H. Eichmann, A. Egbert, S. Nolte, C. Momma, B. Wellegehausen, W. Becker, S. Long, and J. K. McIver, Phys. Rev. A **51**, R3414 (1995).

[3] J. B. Bertrand, H. J. Wörner, H.-C. Bandulet, E. Bisson, M. Spanner, J.-C. Kieffer, D. M. Villeneuve, and P. B. Corkum, Phys. Rev. Lett. **106**, 023001 (2011).

[4] H.-J. Werner, P. J. Knowles, G. Knizia, F. R. Manby, M. Schütz, P. Celani, W. Györffy, D. Kats, T. Korona, R. Lindh, A. Mitrushenkov, G. Rauhut, K. R. Shamasundar, T. B. Adler, R. D. Amos, A. Bernhardsson, A. Berning, D. L. Cooper, M. J. O. Deegan, A. J. Dobbyn, F. Eckert, E. Goll, C. Hampel, A. Hesselmann, G. Hetzer, T. Hrenar, G. Jansen, C. Köppl, Y. Liu, A. W. Lloyd, R. A. Mata, A. J. May, S. J. McNicholas, W. Meyer, M. E. Mura, A. Nicklass, D. P. O'Neill, P. Palmieri, D. Peng, K. Pflüger, R. Pitzer, M. Reiher, T. Shiozaki, H. Stoll, A. J. Stone, R. Tarroni, T. Thorsteinsson, and M. Wang, "MOLPRO, version 2015.1, a package of ab initio programs," (2015).

[5] J. M. L. Martin and A. Sundermann, The Journal of Chemical Physics **114**, 3408 (2001).

[6] F. Neese, Wiley Interdisciplinary Reviews: Computational Molecular Science **8**, e1327 (2017).

[7] O. Smirnova, Y. Mairesse, and S. Patchkovskii, Journal of Physics B: Atomic, Molecular and Optical Physics **48**, 234005 (2015), arXiv:1508.02890.

[8] D. Ayuso, P. Decleva, S. Patchkovskii, and O. Smirnova, Journal of Physics B: Atomic Molecular and Optical Physics **51**, 06LT01 (2018).

[9] D. Ayuso, P. Decleva, S. Patchkovskii, and O. Smirnova, Journal of Physics B: Atomic, Molecular and Optical Physics **51**, 124002 (2018).

[10] D. Baykusheva and H. J. Wörner, Phys. Rev. X **8**, 031060 (2018).

[11] O. Schalk and A. N. Unterreiner, Phys. Chem. Chem. Phys. **12**, 655 (2010).

[12] O. Schalk and P. Hockett, Chemical Physics Letters **517**, 237 (2011).

[13] Y. Chen, A. Rauk, and E. Tschuikow-Roux, The Journal of Physical Chemistry **94**, 6250 (1990).

[14] R. Meyer and H. H. Günthard, The Journal of Chemical Physics **49**, 1510 (1968).

[15] D. T. Colbert and W. H. Miller, Journal of Chemical Physics **96**, 1982 (1992).